





NOEMA Redshift Measurements of Extremely Bright Submillimeter Galaxies Near the GOODS-N

LOGAN H. JONES ¹, MICHAEL J. ROSENTHAL ¹, AMY J. BARGER ^{1,2,3} AND LENNOX L. COWIE ³

¹*Department of Astronomy, University of Wisconsin-Madison, 475 N. Charter Street, Madison, WI 53706, USA*

²*Department of Physics and Astronomy, University of Hawaii, 2505 Correa Road, Honolulu, HI 96822, USA*

³*Institute for Astronomy, University of Hawaii, 2680 Woodlawn Drive, Honolulu, HI 96822, USA*

(Received XXX; Revised YYY; Accepted ZZZ)

Submitted to ApJ

ABSTRACT

We report spectroscopic redshift measurements for three bright submillimeter galaxies (SMGs) near the GOODS-N field, each with SCUBA-2 850 μm fluxes > 10 mJy, using the Northern Extended Millimeter Array (NOEMA). Our molecular linescan observations of these sources, which occupy an ~ 7 arcmin² area outside of the *HST* coverage of the field, reveal that two lie at $z \sim 3.14$. In the remaining object, we detect line emission consistent with CO(7–6), [C I], and H₂O at $z = 4.42$. The far-infrared spectral energy distributions of these galaxies, constrained by SCUBA-2, NOEMA, and *Herschel*/SPIRE, indicate instantaneous star formation rates $\sim 4000 M_{\odot} \text{ yr}^{-1}$ in the $z = 4.42$ galaxy and $\sim 2500 M_{\odot} \text{ yr}^{-1}$ in the two $z \sim 3.14$ galaxies. Based on the sources' CO line luminosities, we estimate $M_{\text{gas}} \sim 10^{11} M_{\odot}$ and find gas depletion timescales of $\tau_{\text{depl}} \sim 50$ Myr, consistent with findings in other high-redshift SMGs. Finally, we show that the two $z \sim 3.14$ sources, which alone occupy a volume $\sim 10 \text{ Mpc}^3$, very likely mark the location of a protocluster of bright SMGs and less dusty optical sources.

Keywords: Submillimeter astronomy (1647) — High-redshift galaxy clusters (2007) — CO line emission (262) — Galaxy evolution (594)

1. INTRODUCTION

Submillimeter galaxies (SMGs) are home to some of the most extreme regions of star formation in the Universe. These highly dust-obscured sources, with far-infrared (FIR) luminosities L_{IR} in excess of $10^{12} L_{\odot}$, have star formation rates (SFRs) of hundreds to thousands of $M_{\odot} \text{ yr}^{-1}$ and typically lie at redshifts $z = 2 - 3$ (e.g., Chapman et al. 2005; Simpson et al. 2014; Neri et al. 2020), though a significant tail in their redshift distribution has been found out to $z > 6$ (e.g., Daddi et al. 2009a,b; Riechers et al. 2020). SMGs are major contributors to the SFR density of the early Universe, accounting for as much as half of all star formation at $z > 1$ (e.g., Cowie et al. 2017; Dudzevičiūtė et al. 2020). The rapid buildup of stellar mass that results from their prodigious SFRs also suggests that SMGs are likely pro-

genitors of compact quiescent galaxies at moderate redshifts and of massive ellipticals locally (e.g., Simpson et al. 2014; Toft et al. 2014).

In addition to being an important phase in massive galaxy evolution, dusty starbursts may also trace the most massive dark matter halos in the early Universe (e.g., Chen et al. 2016; Dudzevičiūtė et al. 2020; Long et al. 2020). In the last ten years, a growing number of $z > 2$ overdensities and protoclusters of galaxies have been discovered through an excess of SMGs and luminous active galactic nuclei (AGNs), each containing several (sometimes > 10) such sources (e.g., Chapman et al. 2009; Daddi et al. 2009a,b; Capak et al. 2011; Walter et al. 2012; Casey et al. 2015; Miller et al. 2018; Oteo et al. 2018; Gómez-Guijarro et al. 2019; Hill et al. 2020; Long et al. 2020; Riechers et al. 2020; Zhou et al. 2020).

However, the relatively short duration ($\lesssim 100$ Myr, e.g., Carilli & Walter 2013) of a dusty starburst phase means that such structures may pose challenges to our understanding of galaxy evolution. Perhaps activation

of the SMG phase is somehow correlated over the volume of a protocluster, though it is unclear how the canonical mechanisms for triggering a starburst in SMGs—gas-rich mergers (e.g., Toft et al. 2014) or the smooth accretion of gas from the surrounding medium (e.g., Tadaki et al. 2018)—could synchronize over large distances and short timescales. Alternatively, the gas depletion timescales τ_{depl} in these environments may be significantly longer than previously thought, up to ~ 1 Gyr in duration (e.g., Casey 2016, and references therein). However, this conflicts with observations that suggest the most massive ellipticals in low-redshift clusters formed most of their stellar mass in short ($\lesssim 1$ Gyr) bursts at high redshift (Thomas et al. 2010). Long τ_{depl} would also imply impossibly massive end-product galaxies, if an SMG were to sustain its $\gtrsim 500 M_{\odot} \text{ yr}^{-1}$ SFR for 1 Gyr.

In any case, the existence of SMG-rich structures in the early Universe provides new and interesting constraints on the growth of individual massive galaxies and the assemblage of large-scale structures. Moreover, the diversity of observed properties of distant protoclusters (e.g., Casey 2016, and references therein) illustrates the need for a statistical sample of such structures if we are to make robust inferences about the growth of galaxy clusters and of massive galaxies across cosmic time.

In the first paper of their SUPER GOODS series, Cowie et al. (2017) presented a deep 450 μm and 850 μm survey of the region around the GOODS-N field using SCUBA-2 on the 15 m James Clerk Maxwell Telescope (JCMT), along with interferometric followup of most of the more luminous SMGs with the Submillimeter Array (SMA). (Note that observations of the field have continued since that published work, and we use the latest images when quoting SCUBA-2 flux densities below.)

Of the six SCUBA-2 sources in the field with 850 μm fluxes greater than ~ 10 mJy, four reside in a small ($\sim 7 \text{ arcmin}^2$) region to the northwest of the field center, just outside the *HST*/ACS and WFC3 footprints of the GOODS (Giavalisco et al. 2004) and CANDELS (Grogin et al. 2011; Koekemoer et al. 2011) surveys; see the upper-right panel of Figure 1. This includes one of the brightest SCUBA-2 850 μm sources in the entire extended GOODS-N with an 850 μm flux density of 18.7 mJy; cf. GN20 (Pope et al. 2005) at 16.3 mJy.

The three brightest SMGs in this grouping appear to be single sources at the resolution of the SMA observations, with the fourth only recently observed (M. Rosenthal et al., in preparation). More than being projected neighbors, their similar 20 cm flux densities, K_s magnitudes, and photometric redshifts $z_{\text{phot}} \sim 3$ (Yang et al. 2014; Hsu et al. 2019) suggest they may also lie at

similar redshifts and may even belong to a single, massively star-forming structure. Two more moderately-bright SCUBA-2 sources, each with $S_{850} > 8$ mJy and $z_{\text{phot}} \sim 3$, also lie in this region.

In this work, we present the first results of a spectroscopic campaign with the IRAM Northern Extended Millimeter Array (NOEMA) to detect CO line emission towards SMGs in this northwest offshoot of the GOODS-N. From these data, we determined spectroscopic redshifts of the three brightest sources and confirmed that two are at nearly identical redshifts. In Section 2, we describe our NOEMA observations and data reduction, along with public multiwavelength imaging for our field. We present the redshifts and observed continuum and line properties of our sources in Section 3. In Section 4, we discuss the nature of these sources as well as their physical properties derived from our NOEMA data and from optical-through-mm spectral energy distribution (SED) fitting. We also discuss the evidence for these sources signposting a galaxy overdensity, concluding that they very likely belong to a protocluster that is relatively rich in SMGs. Finally, we give a brief summary in Section 5. Throughout this work we use a Λ CDM cosmology with $H_0 = 70.5 \text{ km s}^{-1}$, $\Omega_m = 0.27$, and $\Omega_{\Lambda} = 0.73$.

2. DATA

2.1. NOEMA Observations

We targeted the three brightest SCUBA-2 sources in the northwest offshoot of the GOODS-N using the NOEMA interferometer in the compact D configuration (project ID W19DG; PI: Jones). We used two spectral tunings each in the *PolyFix* 2 mm and 3 mm bands, which cover the frequency ranges 78.384–109.116 GHz and 131.384–162.116 GHz. GN-CL-1 and 2 were observed only in the 2 mm band, as 3 mm observations towards these sources had already been carried out in 2019 August; to our knowledge, these data have not yet been published. GN-CL-3 was observed with all four spectral setups. Observations were carried out in track-sharing mode in good weather conditions over the course of 2020 April 10–16, with average atmospheric phase stability of ~ 10 –30% degrees rms and typical precipitable water vapor levels of 1–4 mm. Tracks executed on 2020 April 10 used nine antennas, while all others used ten. In all observations, the quasar 1030+611 was used as the phase and amplitude calibrator. Observations carried out on 2020 April 10 used 0851+202 as the flux calibrator, while all others used LkH α 101. Calibration and imaging of the *uv* data were carried out in GILDAS. We estimate that the absolute flux calibration is accurate at the $\sim 15\%$ level. Images were produced using

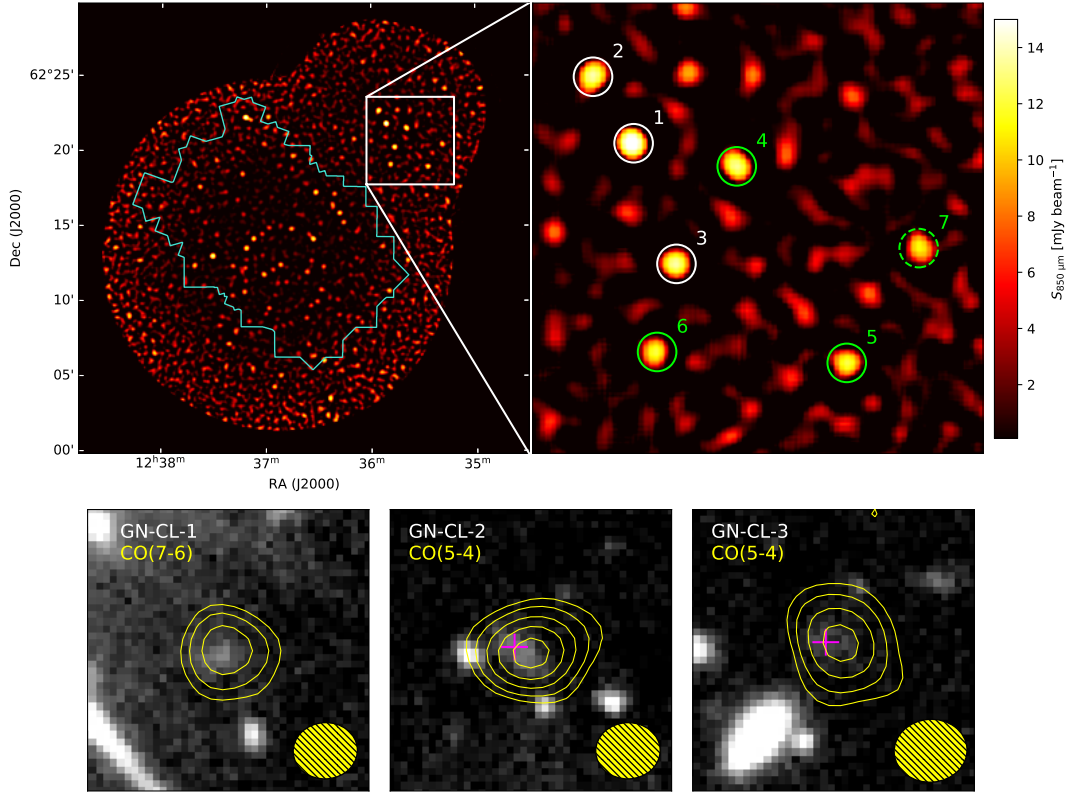


Figure 1. *Top left:* SCUBA-2 850 μm image of the extended GOODS-N. Displayed fluxes include a multiplicative factor of 1.1 to correct for the SCUBA-2 PSF. The blue contour shows the CANDELS *HST*/WFC3 F160W footprint. *Top right:* A zoom-in to the portion of the field that contains our target galaxies (marked by the white box in the top left panel). Our 3 target galaxies are circled in solid white. An additional 3 galaxies with $S_{850} > 8$ mJy, which may also belong to the $z \sim 3.1$ protocluster, are circled in solid green. *Bottom:* CFHT/WIRCAM K_s -band images of GN-CL-1, GN-CL-2, and GN-CL-3. Each panel is $12''$ on a side. Pink crosshairs mark the position of each object’s nearest K -band counterpart (except for GN-CL-1, which has no catalogued counterpart in Hsu et al. (2019) due to its proximity to a bright star). Contours show the 3, 7, 12, 18, and 25σ levels of the CO(7–6) emission line in GN-CL-1 and CO(5–4) in GN-CL-2 and GN-CL-3. In the bottom-right corner of each panel, we show the beam profiles for the CO maps as yellow ellipses.

natural weighting, with typical synthesized beam sizes of $7'' \times 4''$ ($3'' \times 2''.5$) at 3 (2) mm (see bottom panels in Figure 1).

Identification of lines in each tuning and sideband, as well as separation of line- and continuum-only information, were carried out using an iterative process. First, cleaned spectral cubes were binned to ~ 75 km s^{-1} channel widths to better identify potential emission and absorption features. Strong emission features were identified by eye and then masked with the UV_FILTER task in GILDAS/MAPPING using a ~ 800 – 1000 km s^{-1} wide window around the frequency of the line peak. This somewhat aggressive method of line-masking ensures that our continuum measurements remain uncontaminated by strong emission features at the cost of slightly underestimating the continuum flux density. The remaining channels were then collapsed to form our continuum-only images. RMS noise values in a given window were essentially uniform for all sources observed in that win-

dow, ranging from 16–19.8 μJy in the 3 mm band and 23.2–30.1 μJy in the 2 mm band. Continuum-subtracted spectral cubes were created with the UV_BASE task in GILDAS/MAPPING using the same windows as described previously to mask out strong lines.

2.2. Multiwavelength Data

Because *HST* data are not available for our sources, we instead used the compilation of deep ultraviolet (UV), optical, and near-infrared (NIR) photometry of the extended GOODS-N from Hsu et al. (2019) and references therein to constrain the stellar properties of our sources. Specifically, for our SED fits (see Section 4.1), we used Subaru/Suprime-Cam *BVRIZ* data from Capak et al. (2004); CFHT/WIRCAM *JHK_s* data from Wang et al. (2010) and Hsu et al. (2019); and *Spitzer*/IRAC 3.6 μm and 4.5 μm data from Ashby et al. (2013). Two of our three sources (GN-CL-2 and 3) have counterparts in the Hsu et al. (2019) catalog within $1''$ of the

Table 1. NOEMA LINE AND CONTINUUM MEASUREMENTS

Name	R.A. ^a	Dec. ^a	$S_{850\mu\text{m}}^b$ [mJy]	$S_{158.2\text{GHz}}^c$ [mJy]	Line	ν_{obs} [GHz]	z	ν_0 [GHz]	Δv_{FWHM} [km s ⁻¹]	S_{peak} [mJy beam ⁻¹]
GN-CL-1	188.96404	62.36311	18.7±0.5	2.40±0.03	CO(7–6)	148.76	4.422	806.65	513±49	3.1±0.3
					[C I](³ P ₂ – ³ P ₁)	149.24	4.423	809.34	362±63	2.0±0.3
					H ₂ O(2 ₁₁ –2 ₀₂)	138.72	4.421	752.03	430±85	1.2±0.2
GN-CL-2	188.98283	62.37750	11.2±0.5	0.87±0.03	CO(5–4)	138.92	3.148	576.27	369±23	4.3±0.2
GN-CL-3	188.94433	62.33703	11.5±0.6	0.90±0.03	CO(5–4)	139.46	3.132	576.27	500±41	3.0±0.2
					CO(3–2)	83.71	3.131	345.80	459±40	2.0±0.2

NOTE—^aSource positions are from the SMA observations of Cowie et al. (2017) (columns 8 and 9 of their Table 5).

^bThe 850 μm fluxes are from the latest SCUBA-2 images.

^cThis sideband is devoid of obvious spectral features in all of our sources, providing a clean continuum measurement. The flux uncertainties are from the 2D Gaussian fits to the continuum images and do not include systematic uncertainties, such as from absolute flux calibration, which may be $\sim 15\%$.

SMA 870 μm centroid, and we used their photometry directly for these sources. GN-CL-1 is very near a bright ($H = 7.8$) star and thus no nearby optical-NIR counterpart is listed in the Hsu et al. (2019) catalog. Instead, we performed our own aperture photometry on the JHK_s data from Wang et al. (2010) and Hsu et al. (2019) at the SMA position of GN-CL-1. In each band, we measured fluxes in a $2''$ diameter aperture and a local median “background” (which largely comes from the saturated foreground star) in a $2.4''$ – $6''$ diameter annulus, both centered on the SMA position of GN-CL-1. We use the median background values to correct our fluxes for spillover light from the star.

At long wavelengths, we use data from the GOODS-Herschel program of Elbaz et al. (2011) to measure SPIRE 250 μm , 350 μm , and 500 μm fluxes for our sources. Finally, we use the Very Large Array (VLA) 20 cm observations of Morrison et al. (2010) to search for radio counterparts, though the radio fluxes are not included in our SED fits.

3. RESULTS

For GN-CL-1 and GN-CL-2, we extract four continuum flux densities in windows centered at 135.3, 142.8, 150.7, and 158.2 GHz. For GN-CL-3, we extract four at the above frequencies and another four in windows centered at 82.3, 89.8, 97.7, and 105.2 GHz. All of our sources are securely detected in continuum (at the $\gtrsim 4\sigma$ level) in all sidebands of all tunings in which they were observed, though for brevity, we report only the 158.2 GHz flux densities in Table 1, as this sideband is devoid of obvious line emission or absorption in all of our sources and thus provides a clean continuum measurement. As may be expected from their relative 850 μm fluxes, the 158.2 GHz flux densities of GN-CL-2 and 3

are similar at around 0.9 mJy, while that of GN-CL-1 is brighter; we give exact values in Table 1.

We show the full NOEMA spectra of each of our sources in Figure 2, and mark common molecular and atomic transitions in these bands. We do not detect most of the weaker emission features, but GN-CL-1, 2, and 3 all have at least one millimeter emission line detected at $>5\sigma$. We show the spectra from the spaxel with the brightest line emission in Figure 3. Below we discuss the continuum flux densities, line properties, and redshifts of the sources individually.

GN-CL-1: This source is extremely well-detected in continuum, with flux densities rising from 1.3 ± 0.03 mJy (SNR ~ 43) in the 135.3 GHz window to 2.4 ± 0.03 mJy (SNR ~ 80) in the 158.2 GHz window. We detect two strong emission features towards this source at 148.762 and 149.243 GHz and a weaker emission feature at 138.721 GHz, consistent with the frequency ratios of CO(7–6), [C I](³P₂–³P₁), and H₂O(2₁₁–2₀₂) at $z \approx 4.42$. We fit the CO(7–6) and [C I](³P₂–³P₁) lines simultaneously with two Gaussians, without fixing their line ratios, widths, or frequencies relative to one another, and we fit a single Gaussian to the H₂O feature. The three lines have peak flux densities of 3.1 ± 0.3 , 2.0 ± 0.3 , and 1.2 ± 0.2 mJy beam⁻¹ for CO(7–6), [C I](³P₂–³P₁), and H₂O(2₁₁–2₀₂), respectively, with line widths ranging from ~ 360 to 510 km s⁻¹. As we discuss below, this redshift identification shows that GN-CL-1 is not physically associated with either of the remaining two sources.

GN-CL-2: The second brightest SCUBA-2 source in our sample has NOEMA continuum flux densities ranging from 0.41 ± 0.02 mJy in the 135.3 GHz window to 0.87 ± 0.03 mJy in the 158.2 GHz window. We detect a single strong emission line towards GN-CL-2 at 138.917 GHz, with a peak flux density of 4.3 ± 0.2 mJy

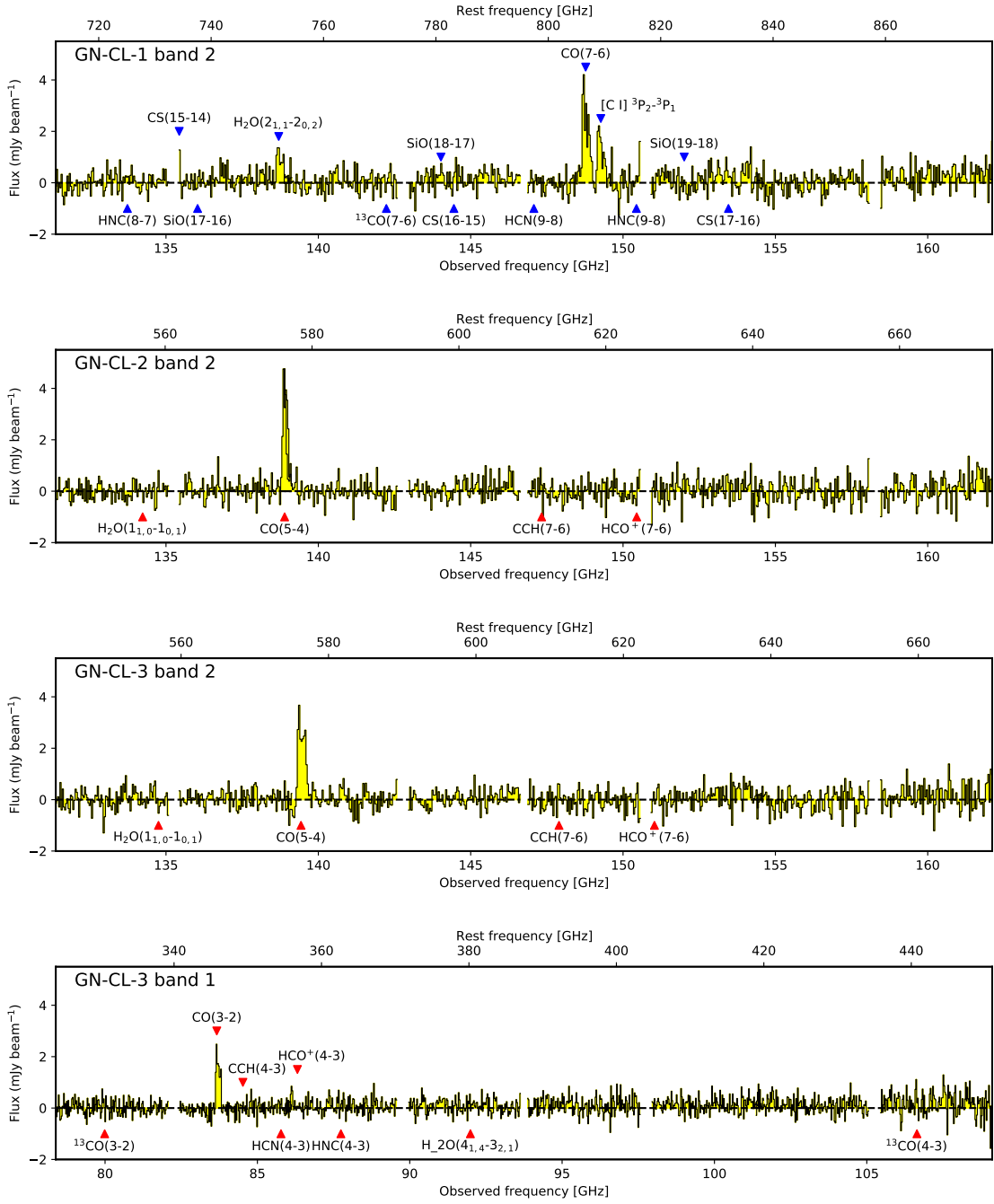


Figure 2. Full millimeter spectra of our three bright SCUBA-2 sources. The source name and band are labeled in the top left corner of each panel. Continuum-subtracted spectra were extracted from the spaxel with the brightest continuum emission. The triangles denote the frequencies of common molecular and atomic emission and absorption lines in the spectral ranges of our observations. Given the rms noise in these spectra, we can only securely identify the CO, H₂O, and [C I] emission lines listed in Table 1. However, for completeness, we also label several weaker transitions that are known to exist in these ranges. Red triangles show commonly observed transitions in SMGs from Spilker et al. (2014). Because that work does not extend to the highest rest-frame frequencies at which we observed GN-CL-1, we mark transitions from the NRAO’s Splatalogue database as blue triangles on its spectrum.

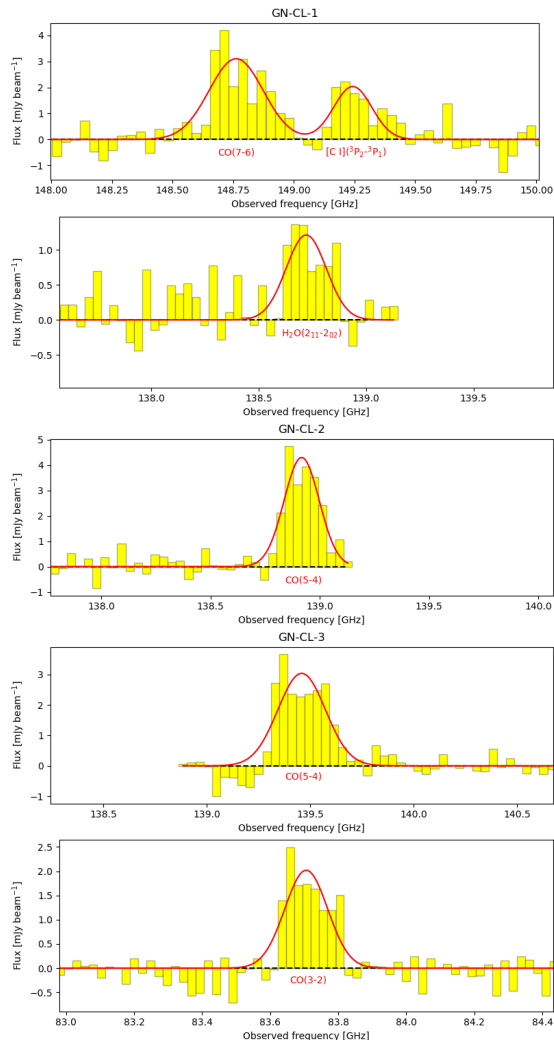


Figure 3. Continuum-subtracted CO or H₂O emission from our three bright SCUBA-2 sources, zoomed in from the full spectra show in Figure 2. Spectra are extracted from the spaxel with the brightest continuum emission. Red lines show Gaussian fits to the data, with the transition labeled in red below the line. The fitted peak flux densities, FWHM velocities, and peak frequencies are listed in Table 1.

beam⁻¹ and a FWHM of ≈ 370 km s⁻¹. For this redshift range, based on the most common millimeter transitions in high-redshift SMGs (e.g., Spilker et al. 2014), a line of this strength is most likely to be CO with $J_{\text{up}} = 4, 5, 6, \text{ or } 7$ at $z = 2.32, 3.15, 3.98, \text{ or } 4.81$, respectively, [C I](1-0) at $z = 2.54$, or H₂O(2₁₁-2₀₂) at $z = 4.41$.

Our near-continuous coverage from 131.4–162.1 GHz allows us to rule out most of these redshift identifications by the non-detection of other strong lines at the expected frequencies. If the feature at 138.917 GHz were CO(4-3) at $z = 2.32$, for example, we would expect to detect [C I](1-0) at $\nu_{\text{obs}} \approx 148.2$ GHz, but no significant line emission is seen there. Redshifts of $z = 3.98$,

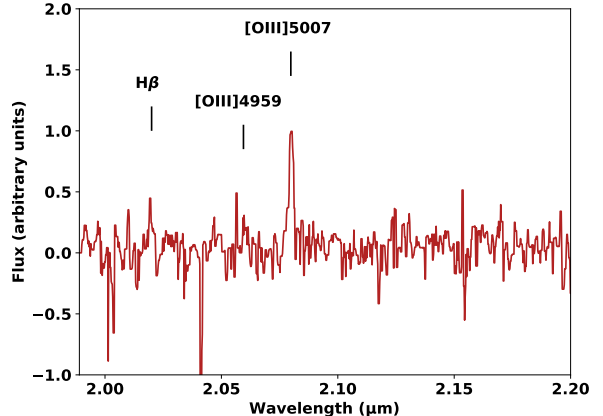


Figure 4. Portion of the Keck/MOSFIRE K -band spectrum of optical source 77630 in the catalog of Hsu et al. (2019), the most likely optical-NIR counterpart to GN-CL-2. The data have been median filtered using a window that is 5 wavelength bins wide. We mark the observed positions of the redshifted [OIII] doublet and H β at $z = 3.15$.

4.41, and 4.81 are similarly ruled out by the absence of strong ($\gtrsim 1$ mJy beam⁻¹) H₂O(2₁₁ - 2₀₂), CO(7-6), and [C I](³P₂-³P₁) emission at their respective expected frequencies.

This leaves CO(5-4) at $z = 3.15$ and [C I](1-0) at $z = 2.54$ as the only viable redshift identifications from the NOEMA data alone. Follow-up Keck/MOSFIRE K -band spectroscopy from M. Rosenthal et al., in preparation, of this source’s nearest optical-NIR counterpart (source 77630 in Hsu et al. 2019, with $K = 22.7$ and a separation of 0 $^{\prime}$.709 from the SMA position of GN-CL-2) finds a redshift of $z = 3.15$ based on the [OIII] doublet and H β (see Figure 4). This confirms the higher redshift identification.

GN-CL-3: GN-CL-3 was the only source we observed in both the 2 mm and 3 mm bands. The nearest optical-NIR counterpart to this SMG (separation of 0 $^{\prime}$.473 from its SMA position) is source 85384 in Hsu et al. (2019). Its millimeter continuum flux densities rise smoothly from 82.5 ± 16 μ Jy in the 82.3 GHz window to 0.9 ± 0.03 mJy in the 158.2 GHz window. We detect strong emission features at 83.706 GHz and 139.458 GHz, consistent with the frequency ratio of CO(3-2) and CO(5-4) at $z \approx 3.13$. Separate Gaussian fits to each of these lines yield peak flux densities of 2.0 ± 0.2 and 3.0 ± 0.2 mJy beam⁻¹, respectively, with FWHM ≈ 480 km s⁻¹. GN-CL-2 and GN-CL-3 are therefore confirmed to lie a mere $\Delta z \sim 0.02$ apart in redshift, with a projected separation of 1.2 Mpc and a 3D separation of 2.7 proper (14.6 comoving) Mpc, if the difference in recession velocities is due only to the Hubble flow. A sphere of diameter equal to the proper

distance between these two galaxies would have a volume of, at most, $\sim 10 \text{ Mpc}^3$. However, as we discuss in the next section, these galaxies very likely belong to a larger overdensity of rare, submillimeter-bright galaxies. If the difference in their redshifts is due to peculiar velocities within a common structure, then the separations quoted above would be overestimates.

Finally, we note that GN-CL-3 appears to have a projected companion about $5''$ to the southeast. This neighboring source is extremely faint in continuum, with a $< 2\sigma$ detection in the $\sim 2 \text{ mm}$ data and completely invisible in the lower-resolution 3 mm data. However, its presence is revealed by a single strong emission feature (peak flux density $\sim 2.5 \text{ mJy}$) at 149.3 GHz . No line emission from an SMG at $z = 3.13$ is expected at this frequency, which suggests that the companion is not associated with GN-CL-3. The line emission is spatially coincident with an optically-bright $z = 0.543$ radio source (Barger et al. 2014), which suggests this line may be CO(2–1).

4. DISCUSSION

4.1. Star Formation Rates, Masses, and Dust Temperatures

The rich photometric data from the rest-frame optical to the radio allow us to constrain the physical properties of these galaxies with SED fitting. We use the Code Investigating GALaxy Emissions (CIGALE, Noll et al. 2009), which calculates SEDs using an energy balance principle, where the energy absorbed by dust in

Table 2. DERIVED PROPERTIES OF CANDIDATE PROTO-CLUSTER MEMBERS

	GN-CL-1	GN-CL-2	GN-CL-3
SFR ^a [$M_{\odot} \text{ yr}^{-1}$]	3900 ± 580	2530 ± 130	2990 ± 770
SFR ₁₀₀ ^b [$M_{\odot} \text{ yr}^{-1}$]	1070 ± 300	630 ± 30	390 ± 140
M_{\star} [$10^{10} M_{\odot}$]	10.7 ± 3.1	5.8 ± 0.3	4.5 ± 1.2
sSFR [Gyr^{-1}]	37 ± 12	44 ± 3	67 ± 25
M_d [$10^9 M_{\odot}$]	4.5 ± 0.4	2.2 ± 0.2	2.0 ± 0.1
$T_{d,\text{char}}$ [K]	33.4 ± 0.8	34.9 ± 0.5	34.8 ± 0.6
M_{gas} [$10^{11} M_{\odot}$]	2.0 ± 0.5	1.3 ± 0.2	1.2 ± 0.2^c
τ_{depl} [Myr]	52 ± 15	51 ± 9	41 ± 13^c
M_{gas}/M_d	45 ± 12	59 ± 11	61 ± 12^c

NOTE—

^aInstantaneous SFR from CIGALE. This row is used to calculate sSFR and τ_{depl} .

^b100 Myr-averaged SFR from CIGALE.

^cGN-CL-3 values use M_{gas} from CO(5–4), but these are consistent within error with values from CO(3–2) (see Section 4.2).

the UV to NIR equals that re-radiated in the MIR to FIR. We use the updated PYTHON version of the code, which has been shown to produce comparable results for high-redshift starbursts to other SED fitting codes (Boquien et al. 2019), to constrain the SFRs, stellar masses, dust masses, and dust temperatures of the three SMGs.

We used Bruzual & Charlot (2003) stellar population libraries with a Chabrier (2003) initial mass function (IMF) for the full range of available metallicities. Stellar spectra are attenuated using a modified Charlot & Fall (2000) dust law with fixed power law indices $\delta_{\text{ISM}} = -0.7$ and $\delta_{\text{BC}} = -1.3$ and a separation age between old and young stellar populations of 10 Myr . We use the dust emission models from Draine et al. (2014), with an input minimum radiation field of $1.0 \leq U_{\text{min}} \leq 50.0^1$ and an input mass fraction of $0.005 \leq \gamma \leq 0.05$ irradiated by $U > U_{\text{min}}$. We fix the radiation field power law slope $\alpha = 2.0$, and we fit for polycyclic aromatic hydrocarbon (PAH) mass fractions $0.47\% \leq q_{\text{PAH}} \leq 3.90\%$. The mean intensity $\langle U \rangle$ is used to derive a characteristic dust temperature, $T_{d,\text{char}} = 18 \text{ K} \times \langle U \rangle^{1/6}$ (Draine et al. 2014), which we report in Table 2.

The properties estimated by CIGALE, especially the SFR, are strongly dependent on the input star formation history (SFH). Given these galaxies have FIR fluxes indicative of ongoing starbursts, we model the SFH as having formed 50–99% of stars by mass in a short, ongoing, flat burst of age $\leq 100 \text{ Myr}$, and the remainder of stars in an exponentially declining SFH of age $0.25\text{--}1.5 \text{ Gyr}$, with e -folding time $250 \text{ Myr} \leq \tau_{\text{main}} \leq 6 \text{ Gyr}$. CIGALE returns a maximum likelihood instantaneous SFR for each galaxy, as well as SFRs averaged over the previous 10 and 100 Myr. Different methods of SFR estimation in the literature report either averaged or instantaneous SFRs, so we report both the instantaneous and 100 Myr-averaged SFR for each galaxy in Table 2. We use the instantaneous SFRs to compute gas depletion times (see Section 4.2). The 100 Myr-averaged SFR is appropriate for comparisons with SFRs output from codes such as MAGPHYS (da Cunha et al. 2015) and works that use it (e.g. Dudzevičiūtė et al. 2020).

We ran CIGALE on FIR to millimeter photometry from *Herschel*/SPIRE, SCUBA-2, and NOEMA, along with observed-frame optical to NIR photometry from Hsu et al. (2019) (for GN-CL-2 and 3) or our own *JHKs* aperture photometry (for GN-CL-1). In addition to the cataloged measurement uncertainties, we included a 10% systematic uncertainty on the absolute photometry/flux calibration in our input flux errors. We fixed the red-

¹ U has units of 1 Habing = $1.6 \times 10^{-3} \text{ erg cm}^{-2} \text{ s}^{-1}$

shifts at the spectroscopic redshift of each source; that is, $z_{spec} = 4.42$ for GN-CL-1 and $z_{spec} = 3.14$ for GN-CL-2 and GN-CL-3. We show the best-fit SEDs for the three SMGs in Figure 5.

Based on its best-fitting SED, GN-CL-1 has an 8–1000 μm luminosity $L_{\text{IR}} \approx 1.1 \times 10^{13} L_{\odot}$, making it a high-redshift hyper-luminous infrared galaxy (HyLIRG). Its instantaneous SFR = $3900 \pm 580 M_{\odot} \text{ yr}^{-1}$ is one of the largest in the field. With $\sim 10^{11} M_{\odot}$ of stars already in place by $z = 4.42$, this source is the likely progenitor of a massive elliptical at $z \approx 0$. GN-CL-2 and GN-CL-3 are also massive star-forming galaxies, with 8–1000 μm luminosity $L_{\text{IR}} \approx 5 \times 10^{12} L_{\odot}$, comparable to nearby ultraluminous infrared galaxies, and instantaneous SFR $\approx 2500 M_{\odot} \text{ yr}^{-1}$. The similarities between GN-CL-2 and GN-CL-3, as well as the difference in their values compared with GN-CL-1, are consistent with rough expectations from the 850 μm flux densities.

4.2. Gas Mass and Depletion Timescale

Molecular hydrogen’s low emissivity makes it hard to detect even in nearby galaxies, so the luminosity of the CO(1–0) emission line is often used as a proxy for the mass of molecular hydrogen, M_{H_2} . We follow the methodology of Bothwell et al. (2013) to convert our higher J CO transitions to CO(1–0), and subsequently into a molecular gas mass for each galaxy, M_{gas} .

We compute the line luminosity L'_{CO} using the standard relation from Solomon & Vanden Bout (2005):

$$L'_{\text{CO}} = 3.25 \times 10^7 \times S_{\text{CO}} \Delta V \nu_{\text{obs}}^{-2} D_L^2 (1+z)^{-3}, \quad (1)$$

where L'_{CO} is the line luminosity with units $\text{K km s}^{-1} \text{ pc}^2$, $S_{\text{CO}} \Delta V$ is the integrated line luminosity in Jy km s^{-1} , ν_{obs} is the observed line frequency in GHz, and D_L is the luminosity distance in Mpc. We take $S \Delta V$ to be the area underneath the Gaussian fits to each detected CO line and convert our measured luminosities from higher J lines to CO(1–0) using Table 4 of Bothwell et al. (2013). Errors on L'_{CO} are dominated by errors on $S \Delta V$ and on the J -conversion factors $r_{76/10}$, $r_{54/10}$, and $r_{32/10}$. We assume an $L'_{\text{CO}(1-0)}$ to M_{H_2} conversion factor $\alpha = 1 M_{\odot} (\text{K km s}^{-1} \text{ pc}^2)^{-1}$. Finally, we multiply a correction of $M_{\text{gas}} = 1.36 M_{\text{H}_2}$ to account for the addition of helium.

For a given SFR and M_{gas} , the depletion timescale is approximately given by

$$\tau_{\text{depl}} = \frac{M_{\text{gas}}}{\text{SFR}}. \quad (2)$$

We list the gas masses and depletion times for our galaxies in Table 2. For GN-CL-3, which has both CO(5–4)

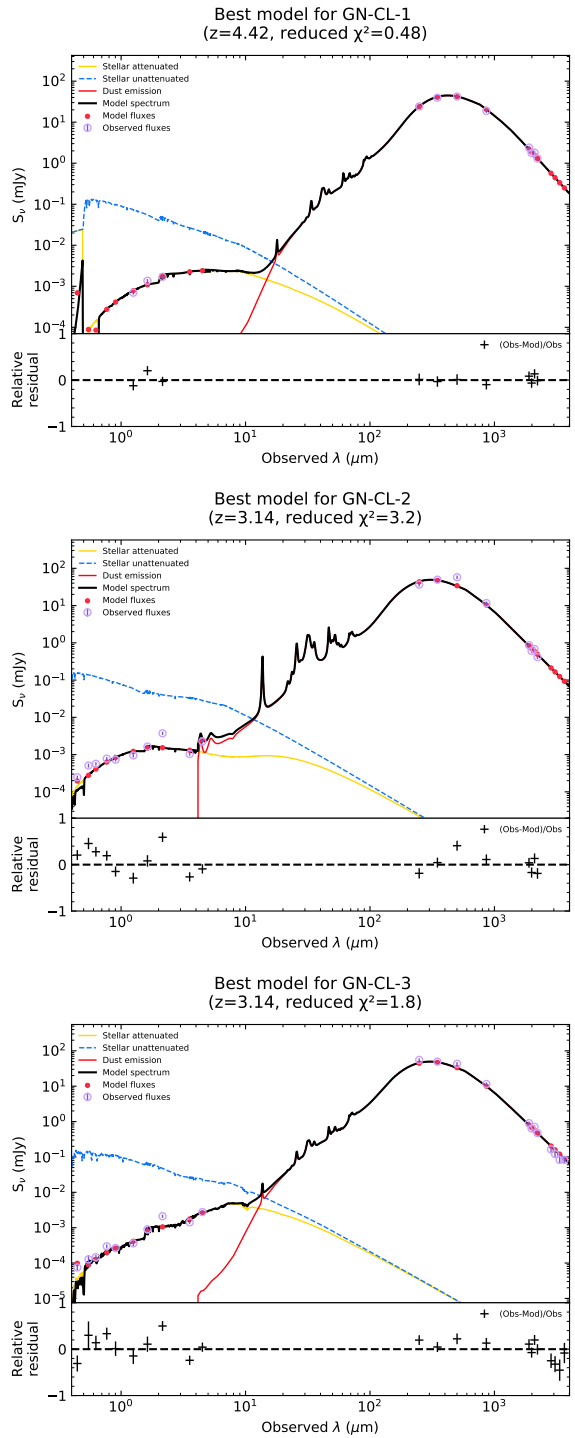


Figure 5. Best-fit SEDs from CIGALE for each SMG. The black curve shows the total SED, while the red and yellow curves show the relative contributions to the SED of the dust and the attenuated stellar emission, respectively. The purple and red dots show the measured and fit fluxes, respectively.

and CO(3–2) detections, we show values for CO(5–4) for consistency with GN-CL-2, but the values derived from both lines are consistent within errors². The depletion times of ~ 50 Myr are consistent with values for other high-redshift SMGs based on high- J_{up} CO lines (e.g., Casey 2016). Based on the calculations in Casey (2016), we would not be likely to observe two SMGs in the same structure with such short depletion times, though we note that values of τ_{depl} are dependent on the SFR measurement methods used, and, by extension, the assumed SFH, IMF, and conversion factor, α .

4.3. (Sub)Millimeter Evidence of a Protocluster

As mentioned previously, the three SMGs we targeted with NOEMA are part of a larger grouping of seven bright SCUBA-2 sources to the northwest of the *HST* coverage of the GOODS-N. One is confirmed by our NOEMA observations to lie at high redshift ($z = 4.42$), while another (source 7 in Figure 1) has a *U*-band counterpart and $z_{\text{phot}} = 1.58$, making it unlikely to belong to the same $z \approx 3.14$ halo as GN-CL-2 and GN-CL-3. The remaining three sources (4, 5, and 6 in Figure 1) have SCUBA-2 850 μm fluxes of 9.8 mJy, 8.6 mJy, and 8.2 mJy, respectively. NOEMA redshift scans of these additional sources, which will determine whether they are part of the same system as GN-CL-2 and GN-CL-3, will be carried out in 2021. In the meantime, we can use the known number counts of bright SMGs to estimate the probability that these sources belong to a larger structure or protocluster.

The S2COSMOS survey of Simpson et al. (2019) presents number counts of SCUBA-2 850 μm sources in the COSMOS field over 2.6 deg^2 , with a typical 1σ noise level of $1.2 \text{ mJy beam}^{-1}$ in the central region of the field. Their incompleteness-corrected cumulative number counts (their Table 2) suggest that one can expect $61.9_{-7.7}^{+7.2}$ sources per deg^2 ($0.017_{-0.002}^{+0.002} \text{ arcmin}^{-2}$) at a flux density $S_{850} > 7.7 \text{ mJy}$. However, there are seven $S_{850} > 8 \text{ mJy}$ galaxies in the northwest offshoot of the GOODS-N that occupy an area only $\sim 4.6 \times 4.1 \text{ arcmin}^2$ in size, for a cumulative source density of $N(S_{850} > 8 \text{ mJy}) = 0.371 \text{ arcmin}^{-2}$. If we assume that the positions of bright SMGs are completely random on the plane of the sky and uncorrelated in redshift space, then the number counts in Simpson et al. (2019) suggest that we should expect an average of just 0.321 sources with $S_{850} > 8$ in a given $4.6 \times 4.1 \text{ arcmin}^2$ area, a factor of 21.8 lower than what is observed in our field. Even removing

sources 1 and 7 (for a total of 5 galaxies across a $4 \times 4 \text{ arcmin}^2$ area) yields a projected overdensity 14 times higher than what would be expected if the remaining sources were not part of a single structure.

Alternatively, let us assume that whether or not a bright SMG is seen in a unit area is a Poissonian process so that we can use small number statistics (Gehrels 1986) to determine the raw likelihood of seeing multiple randomly-distributed $S_{850} > 8 \text{ mJy}$ sources in an 18.9 arcmin^2 box. Specifically, if we treat GN-CL-2 and GN-CL-3 as a single system due to their nearly-identical redshifts, then we may compute the chances of observing $2 < N < 6$ projected systems via $P(N; 0.321) = \frac{\lambda^N e^{-\lambda}}{N!}$, where $\lambda = 0.321$ is the mean expected number of sources in a $4.6 \times 4.1 \text{ arcmin}^2$ area. As may be expected, the probability of such a projection drops rapidly with increasing N , falling from 3.7% at $N = 2$ to $1.1 \times 10^{-4}\%$ at $N = 6$. For $N = 5$ (6), only ~ 2500 (160) such projections are expected to be seen across the entire sky.

However, we know from the combination of our NOEMA observations and the UV through radio photometry of Hsu et al. (2019) that sources 1 and 7 are, indeed, a chance projection with one another and with sources 2 and 3. In other words, all three systems are independent “events” such that N is at least 3. If even one of the remaining three bright SMGs is *also* a chance projection with these systems, then we begin to move into a regime of such extraordinarily low probability that it defies our assumption of independent and physically unassociated systems.

4.4. Optical Evidence of a Protocluster

The region we consider in this work is well outside the *HST* coverage of the GOODS-N. Thus, spectroscopic followup is extremely incomplete, even for relatively bright objects, compared to the GOODS/CANDELS portion of the field. Within a $5'$ radius of the mean position of all seven bright SMGs, there are 316 (2949) sources with R magnitudes brighter than 22 (25), of which only 3 (8) objects have a published spectroscopic redshift in the multiband catalog of Hsu et al. (2019), with none at $z > 2$.

In M. Rosenthal et al., in preparation, we will use our Keck/MOSFIRE spectroscopy of optical-NIR sources in the northwest region of the GOODS-N, together with our existing and upcoming NOEMA data, to characterize the $z \approx 3.14$ protocluster. For now, we use the multiband catalog of Hsu et al. (2019) to see whether evidence of an optical overdensity is present based on photometric redshifts only. We restrict to objects with Kron R magnitudes brighter than 25 and R magnitude errors fainter than 26.75, corresponding to a $> 5\sigma$ detec-

² Specifically, $M_{\text{gas}} = (12.3 \pm 2.3) \times 10^{10} M_{\odot}$ and $\tau_{\text{depl}} = 41 \pm 13 \text{ Myr}$ for CO(5–4), and $M_{\text{gas}} = (12.8 \pm 2.7) \times 10^{10} M_{\odot}$ and $\tau_{\text{depl}} = 43 \pm 14 \text{ Myr}$ for CO(3–2).

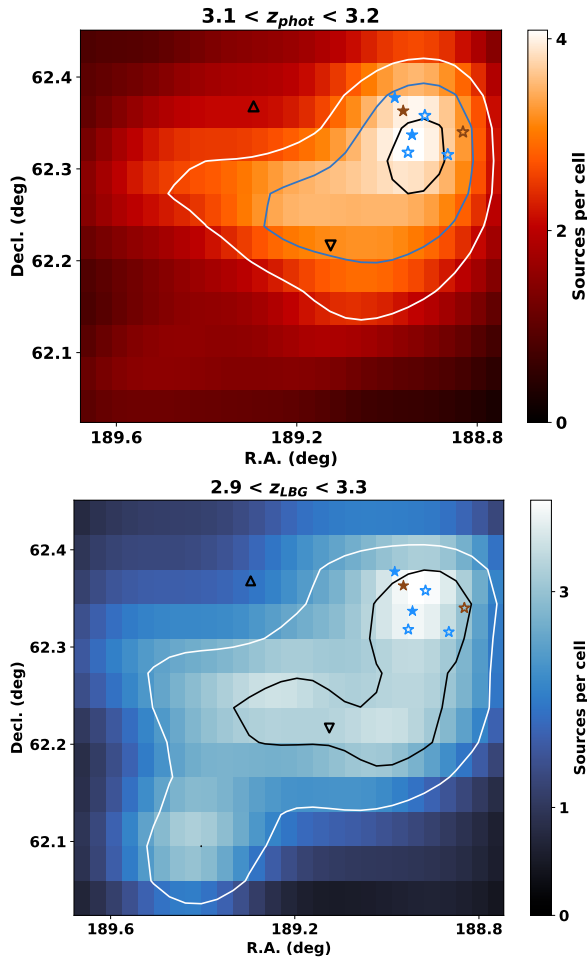


Figure 6. Projected 2D density of all sources in the extended GOODS-N with $3.1 < z_{phot} < 3.2$ in Hsu et al. (2019) (*top*) and those in the interval $2.9 < z_{phot} < 3.3$ that meet the LBG criteria of Capak et al. (2004) (*bottom*). In both panels, a Gaussian kernel density estimate has been applied, and each cell is 2×2 arcmin². Contours on the top (bottom) panel indicate regions where the source density is 3σ , 4σ , and 5σ (2σ and 3σ) higher than the mean in the CANDELS portion of the field. Filled stars show the positions of SMGs observed as part of this work (blue if they are spectroscopically confirmed to lie at $z \sim 3.14$, and brown otherwise). Blue open stars show the positions of other $S_{850} > 8$ mJy SMGs in the region that do not yet have spectroscopic confirmation but may belong to the overdensity. The brown open star is an SMG with a bright U -band counterpart and $z_{phot} = 1.58$. Upward- and downward-pointing open triangles, respectively, mark the positions of the GN20 overdensity (Pope et al. 2005; Daddi et al. 2009a) and the $z = 1.99$ SMG-rich protocluster of Chapman et al. (2009).

tion. We further restrict to regions where the per-pixel J -band flux uncertainties are less than twice the median rms in the central part of the field. This results in the loss of 139 arcmin² of the JHK_s survey area but also removes the bulk of spurious or extremely noisy sources

near the edge of the field. Over the redshift interval $3.1 < z_{phot} < 3.2$, we find a mean density of 0.58 galaxies per arcmin². However, when we perform a similar analysis in an area of radius $4'$ centered on the bright SMG overdensity, we find a mean density of 0.89 galaxies per arcmin². The total number of objects in the overdense region is 45 compared with an expected value of 29.

We next compare the distribution of the number of sources in $1'$ square cells in the full field with that in an $8'$ square area centered on the SMGs (64 cells). A one-tailed Mann-Whitney test of these two samples yields a p value of 0.0014, which implies that they are not drawn from the same distribution and that the optical-NIR overdensity is statistically significant.

For visualization purposes, we show in the top panel of Figure 6 a 2D histogram of the source density in this narrow photometric redshift interval. This density map has been “smoothed” using a Gaussian kernel density estimate with $2' \times 2'$ bins. We note a clear maximum in the density of optical sources that is coincident with the grouping of bright SMGs.

As an additional check, we examine the spatial distribution of candidate Lyman Break Galaxies (LBGs) across the extended GOODS-N in the bottom panel of Figure 6. We use the color criteria of Capak et al. (2004) to select LBGs in the redshift interval $2.9 < z_{phot} < 3.3$. While the photometric redshift interval is too broad to constrain the number of LBGs that may belong to a single, coherent structure at $z \approx 3.14$, we nevertheless note that the maximum density of LBGs is again coincident with the (projected) overdensity of bright SMGs (see the bottom panel of Figure 6).

Finally, we note that the $\sim 0^{\circ}07 \times 0^{\circ}07$ angular extent of our extremely bright SMG overdensity is intermediate in size compared to other high-redshift, SMG-rich protoclusters in the literature. For example, this structure is quite compact compared to the $z = 1.99$ structure in the GOODS-N (Chapman et al. 2009, $0^{\circ}17 \times 0^{\circ}17$), the SSA22 protocluster at $z = 3.1$ (Steidel et al. 1998, $0^{\circ}33 \times 0^{\circ}50$), and the $z = 5.18$ HDF850.1 overdensity (Walter et al. 2012, $0^{\circ}10 \times 0^{\circ}13$). However, it is more extended than the GN20 overdensity (Pope et al. 2005; Daddi et al. 2009a,b, $0^{\circ}01 \times 0^{\circ}01$) and the Distant Red Core (Oteo et al. 2018; Ivison et al. 2020, $0^{\circ}02 \times 0^{\circ}02$), both at $z \sim 4$. We defer a fuller discussion of the total SFR, stellar mass, halo mass, and physical extent to M. Rosenthal et al., in preparation.

5. SUMMARY

We report the results of a millimeter spectroscopic campaign with NOEMA to measure redshifts for three of

the 850 μm -brightest SMGs in the extended GOODS-N, which lie in a close (projected) grouping. We determined unambiguous spectroscopic redshifts for two of our three targets using the NOEMA data alone (GN-CL-1 at $z = 4.42$ and GN-CL-3 at $z = 3.13$) and for the remaining target using both NOEMA and Keck/MOSFIRE spectroscopy (GN-CL-2 at $z = 3.15$). With nearly identical redshifts, GN-CL-2 and 3 are likely part of a single system and may signpost an overdensity of galaxies at $z \approx 3.14$. More importantly, there are three more bright, neighboring SMGs which, based on number counts and simple probability estimates, are extremely likely to belong to the same structure, constituting a protocluster of short-lived SMGs in the high-redshift Universe. Finally, our best-fit SEDs suggest that GN-CL-1, one of the brightest SCUBA-2 850 μm sources in the extended GOODS-N field, is an extremely FIR-luminous, high-redshift dusty starburst with $\sim 10^{11} M_{\odot}$ already formed when the Universe was only 1.4 Gyr old.

ACKNOWLEDGMENTS

We thank the anonymous referee for a useful report that helped us to improve the manuscript. We gratefully acknowledge support for this research from a Wisconsin Space Grant Consortium Graduate and Professional Research Fellowship (L.J.), NASA grant NNX17AF45G (L.L.C.), the William F. Vilas Estate (A.J.B.), and the Kellett Mid-Career Award from the University of Wisconsin-Madison Office of the Vice Chancellor for Research and Graduate Education with funding from the Wisconsin Alumni Research Foundation (A.J.B.).

This work is based on observations carried out under project number W19DG with the IRAM NOEMA Interferometer. IRAM is supported by INSU/CNRS (France), MPG (Germany) and IGN (Spain). L. Jones thanks Vinod Arumugam for many helpful discussions on the reduction and processing of NOEMA observations.

Facilities: Subaru (Suprime-Cam), JCMT (SCUBA-2), SMA, NOEMA, *Herschel*, JVLA

Software: `astropy` ([Astropy Collaboration et al. 2018](#))

REFERENCES

- Astropy Collaboration, Price-Whelan, A. M., Sipőcz, B. M., et al. 2018, *AJ*, 156, 123
- Ashby, M. L. N., Willner, S. P., Fazio, G. G., et al. 2013, *ApJ*, 769, 80
- Barger, A. J., Cowie, L. L., Chen, C.-C., et al. 2014, *ApJ*, 784, 9
- Boquien, M., Burgarella, D., Roehlly, Y., et al. 2019, *A&A*, 622, A103
- Bothwell, M. S., Smail, I., Chapman, S. C., et al. 2013, *MNRAS*, 429, 3047
- Bruzual, G. & Charlot, S. 2003, *MNRAS*, 344, 1000
- Calzetti, D., Armus, L., Bohlin, R. C., et al. 2000, *ApJ*, 533, 682
- Capak, P., Cowie, L. L., Hu, E. M., et al. 2004, *AJ*, 127, 180
- Capak, P. L., Riechers, D., Scoville, N. Z., et al. 2011, *Nature*, 470, 233
- Carilli, C. L. & Walter, F. 2013, *ARA&A*, 51, 105
- Casey C. M., Narayanan D., & Cooray A., 2014, *Phys. Rep.*, 541, 45
- Casey, C. M., Corray, A., Capak, P. et al. 2015, *ApJL*, 808, 33
- Casey, C. M. 2016, *ApJ*, 824, 36
- Chabrier, G. 2003, *PASP*, 115, 763
- Chapman S. C., Blain A. W., Smail I., & Ivison R. J., 2005, *ApJ*, 622, 772
- Chapman, S. C., Blain, A., Iyata, R., et al. 2009, *ApJ*, 691, 560
- Charlot, S. & Fall, S. M. 2000, *ApJ*, 539, 718
- Chen, C.-C., Smail, I., Ivison, R. J., et al. 2016, *ApJ*, 820, 82
- Cowie, L. L., Barger, A. J., Hsu, L.-Y., et al. 2017, *ApJ*, 837, 139
- da Cunha, E., Walter, F., Smail, I. R., et al. 2015, *ApJ*, 806, 110.
- Daddi, E., Dannerbauer, H., Stern, D., et al. 2009a, *ApJL*, 694, 1517
- Daddi, E., Dannerbauer, H., Krips, M., et al. 2009b, *ApJL*, 695, 176
- Draine, B. T., Aniano, G., Krause, O., et al. 2014, *ApJ*, 780, 172
- Dudzevičiūtė, U., Smail, I., Swinbank, A. M., et al. 2020, *MNRAS*, 494, 3828
- Elbaz, D., Dickinson, M., Hwang, H. S., et al. 2011, *A&A*, 533, A119
- Gehrels, N. 1986, *ApJ*, 303, 336
- Giavalisco, M., Ferguson, H. C., Koekemoer, A. M., et al. 2004, *ApJ*, 600, L93
- Gómez-Guijarro, C., Riechers, D. A., Pavesi, R. et al. 2019, *ApJ*, 872, 117
- Grogin, N. A., Kocevski, D. D., Faber, S. M., et al. 2011, *ApJS*, 197, 35
- Hill, R., Chapman, S. C., Scott, D., et al. 2020, *MNRAS*, 495, 3124
- Hsu, L.-T., Lin, L., Dickinson, M., et al. 2019, *ApJ*, 871, 233
- Ivison, R. J., Biggs, A. D., Bremer, M., et al. 2020, *MNRAS*, 496, 4358
- Koekemoer, A. M., Faber, S. M., Ferguson, H. C., et al. 2011, *ApJS*, 197, 36
- Lo Faro, B., Buat, V., Roehlly, Y., et al. 2017, *MNRAS*, 472, 1372
- Long, A. S., Cooray, A., Ma, Jingzhe, et al. 2020, *ApJ*, 898, 133
- Miller, T. B., Chapman, S. C., Aravena, M., et al. 2018, *Nature*, 556, 469
- Morrison, G. E., Owen, F. N., Dickinson, M., et al. 2010, *ApJS*, 188, 178
- Neri, R., Cox, P., Omont, A., et al. 2020, *A&A*, 635, A17
- Noll, S., Burgarella, D., Giovannoli, E., et al. 2009, *A&A*, 507, 1793
- Oteo I., Ivison, R. J., Dunne, L., et al., 2018, *ApJ*, 856, 72
- Pope, A., Borys, C., Scott, D., et al. 2005, *MNRAS*, 358, 149
- Riechers, D. A., Hodge, J. A., Pavesi, R. et al. 2020, *ApJ*, 895, 81
- Simpson, J. M., Swinbank, A. M., Smail, I., et al. 2014, *ApJ*, 788, 125

- Simpson, J. M., Smail, I., Swinbank, A. M., et al. 2019, *ApJ*, 880, 43
- Solomon, P. M. & Vanden Bout, P. A. 2005, *ARA&A*, 43, 677
- Spilker, J. S., Marrone, D. P., Aguirre, J. E., et al. 2014, *ApJ*, 785, 149
- Steidel, C. C., Adelberger, K. L., Dickinson, M., et al. 1998, *ApJ*, 492, 428
- Toft, S., Smolčić, V.; Magnelli, B. et al. 2014, *ApJ*, 782, 68
- Tadaki, K., Iono, D., Yun, M. S., et al. 2018, *Nature*, 560, 613
- Tasca, L. A. M., Le Fèvre, O., Hathi, N. P., et al. 2015, *A&A*, 581, A54
- Thomas D., Maraston C., Schawinski K., et al. 2010, *MNRAS*, 404, 1775
- Walter, F., Decarli, R., Carilli, C., et al. 2012, *Nature*, 486, 233
- Wang, W.-H., Cowie, L. L., Barger, A. J., Keenan, R. C., & Ting, H.-C. 2010, *ApJS*, 187, 251
- Yang, G., Xue, Y. Q., Luo, B. et al. 2014, *ApJS*, 215, 27
- Zhou, L., Elbaz, D., Franco, M., et al. 2020, *A&A*, 642, A155